Passive mode control in the recirculating planar magnetron

Matthew Franzi,[1] Ronald Gilgenbach,[1] Y. Y. Lau,[1] Brad Hoff,[2] Geoff Greening,[1] and Peng Zhang[1]
[1]*Plasma, Pulsed Power, and Microwave Laboratory, Nuclear Engineering and Radiological Sciences Department, University of Michigan, Ann Arbor, Michigan 48109-2104, USA*
[2]*Air Force Research Laboratory, Kirtland AFB, New Mexico 87117, USA*

(Received 25 December 2012; accepted 26 February 2013; published online 19 March 2013)

Preliminary experiments of the recirculating planar magnetron microwave source have demonstrated that the device oscillates but is susceptible to intense mode competition due, in part, to poor coupling of RF fields between the two planar oscillators. A novel method of improving the cross-oscillator coupling has been simulated in the periodically slotted mode control cathode (MCC). The MCC, as opposed to a solid conductor, is designed to electromagnetically couple both planar oscillators by allowing for the propagation of RF fields and electrons through resonantly tuned gaps in the cathode. Using the MCC, a 12-cavity anode block with a simulated 1 GHz and 0.26 c phase velocity (where c is the speed of light) was able to achieve in-phase oscillations between the two sides of the device in as little as 30 ns. An analytic study of the modified resonant structure predicts the MCC's ability to direct the RF fields to provide tunable mode separation in the recirculating planar magnetron. The self-consistent solution is presented for both the degenerate even (in phase) and odd (180° out of phase) modes that exist due to the twofold symmetry of the planar magnetrons. © *2013 American Institute of Physics*. [http://dx.doi.org/10.1063/1.4794967]

I. INTRODUCTION

The recirculating planar magnetron (RPM), shown in Fig. 1, is a new type of cavity magnetron designed to provide several geometrical advantages over its cylindrical counterpart. These advantages include enhanced heat dissipation in the anode, reduced loading on the cathode, higher beam currents, and favorable scaling of magnetic field volume.[1,2]

While anticipated to improve efficiency and peak power, the RPM geometry introduces some additional complexity to the operation of the device, as compared to the purely cylindrical alternative. Initial designs of the RPM have demonstrated that the device oscillates but is susceptible to weak electromagnetic coupling between the two planar slow-wave structures which might cause several deleterious phenomena. Two of the primary complications are:

(1) Cross-oscillator mode competition (even and odd mode development).[3]
(2) Phase drifting and offsets between oscillators during operation, which has been shown in both simulations[4] and demonstrated in experiments as depicted in Fig. 2.

This paper proposes the mode control cathode (MCC), shown in Figs. 3(a) and 3(b), as a means of alleviating mode competition and eliminating phase mismatches by improving both mode separation and cross oscillator coupling.

II. COUPLING IN THE RPM

The RPM (Fig. 1) is more appropriately regarded as two distinct arrays of planar oscillators, in contrast to a conventional cylindrical magnetron with a single uniform slow wave structure.[1] The two resonant arrays, which are predominantly isolated by the conducting boundary at the cathode, are only coupled at either end of the device by cylindrical smooth-bore sections. These adjoining regions, designed primarily to preserve beam current, often fail to maintain complete synchronism of space charge bunches from one oscillator to the other. The "detuned" electron beam must then "re-bunch" as it traverses through each planar slow-wave structure, which may adversely affect RF communication from the opposing side. The partially isolated oscillators often fail to achieve a global locked mode during operation and instead exhibit mode competition and beating between each of the separate oscillators.

Enhanced coupling has been proposed through several other potential mechanisms including continuous slow-wave structures (cylindrical and planar cavities), capacitively coupled anode cavities (inverted magnetron configuration only), and anode strapping although most of these alternatives fail to completely address the issue in a convenient manner.[1,5–9] Resonant slow-wave structures are difficult to match across multiple sections and can support dissimilar mode development between cylindrical and planar oscillators. These structures also require larger area anodes and increase the complexity of maintaining balanced cavity loading while extracting power. Capacitively coupled cavities, in an inverted magnetron configuration, require resonantly tuned slots across the interior of the anode and therefore must take the place of or coexist with extraction waveguides. Lastly, anode strapping has been shown to induce breakdown across oppositely polarized vanes in relativistic magnetron operating regimes.[9,10]

The MCC presents a potentially more effective and convenient means of improving cross-oscillator coupling in the RPM by enabling the cathode to resonantly propagate the RF fields and electron bunches from one oscillator to the other during operation.

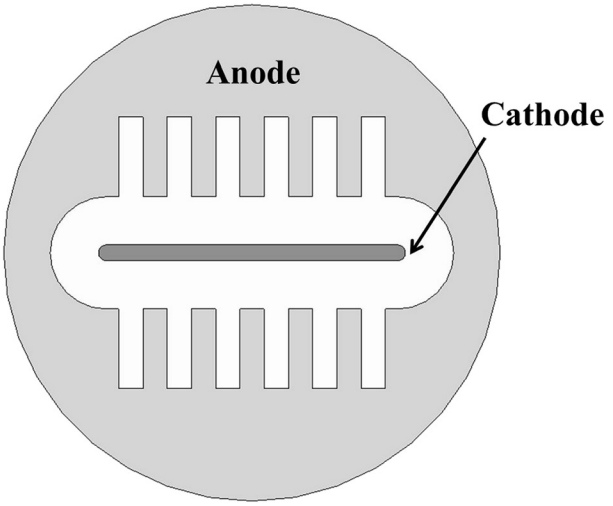

FIG. 1. A 2D rendered image of the RPM-12a anode structure viewing the front of the device. The center plate is the cathode; the anode periodic structures are above and below the cathode, and the axial magnetic field points out of the page.

The periodically slotted geometry of the MCC is similar in form to a linear version of the transparent cathode, which has been shown to improve efficiency and start up time in relativistic cylindrical magnetrons.[11] The MCC, however, utilizes tuned waveguides in the electrode to act as an electromagnetic coupler for the opposing slow wave structures rather than purely a mechanism to maximize the static electric fields at the surface of the conductor. The MCC, by design, facilitates a global mode structure which extends across the horizontal plane of symmetry in the RPM. Additionally, counter-propagating electron beams denoted by the ("thick") arrows in Fig. 3(a) readily circulate through the cathode waveguides acting to both excite and prime the desired RF mode of both oscillator sets simultaneously. The waveguide slots in the cathode were placed under every cavity of the slow wave structure to maximize both the magnitude of the transverse electric field, E_y (see Fig. 4 for coordinates), reaching the opposing oscillator as well as to enhance emission priming of the π-mode.[12] The even π-mode electric field configuration shown in Fig. 3(b) can also lead to cross-oscillator "self-focusing," wherein space charge beneath a cavity exhibits the same $E_{RF} \times B$ drift direction regardless of its position in (x).

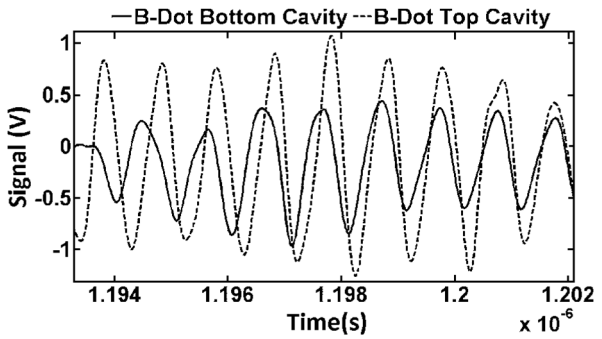

FIG. 2. Experimental b-dot signal of horizontally symmetric cavities on the top and bottom oscillator in the recirculating planar magnetron.

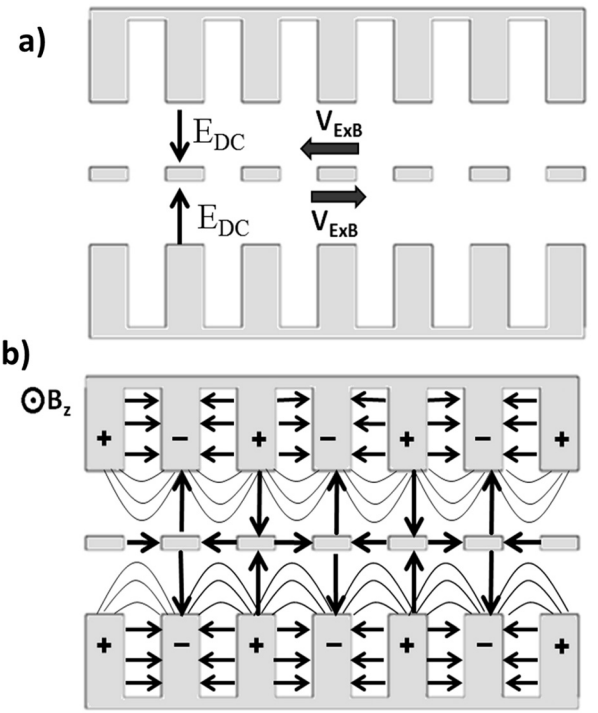

FIG. 3. (a) RPM slow wave structure with slotted mode control cathode; black arrows illustrate externally applied electrostatic fields, thick arrows represent the $E \times B$ drift of the electron beam. (b) RPM slow wave structure with the slotted mode control cathode; black lines illustrate the RF electric field configuration of the even π-mode.

III. DISPERSION RELATION

The RPM is susceptible to a high degree of mode competition, particularly from the closely spaced degenerate even and odd π-modes that share the same guided wavelength in the planar magnetron.[3,6] The MCC, which possesses greater geometric flexibility in size and shape than the standard solid cathode, can mitigate this mode competition by offering a viable mechanism to tune the resonant cavity of the RPM independently from the anode. The mode separation provided by the MCC is solved for analytically by evaluating the full dispersion relation as a function of the cathode's tunable parameters: cathode height (h_2), slot width

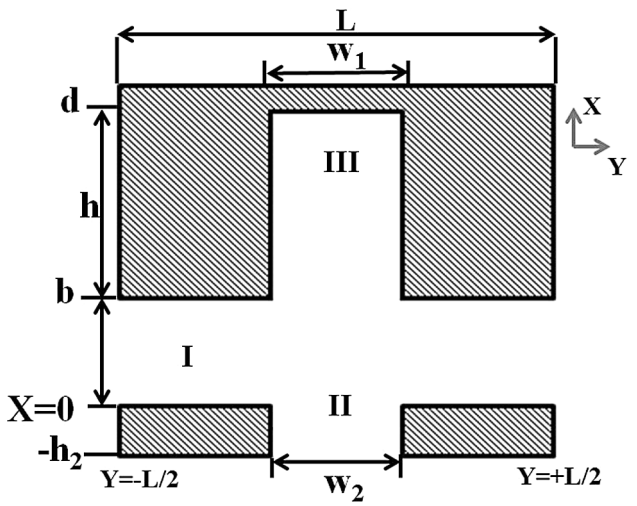

FIG. 4. The upper half of a single 2D resonant cavity in the RPM representing the simplified modular geometry used to solve for the MCC dispersion relation.

(w_2), and AK gap (b). Figure 4 illustrates the analytic setup of a single cavity in an infinite array (in y) with period L. The operating mode of the device is determined by both the propagation constant in (y) for the n*th* spatial harmonic β_n (where $\beta_n = \beta_0 + 2\pi n/L$, β_0 is the fundamental harmonic), which identifies the phase shift per cavity, as well as the boundary condition along the horizontal symmetry plane ($x = -h_2$), which defines either the even or odd mode planar degeneracy in the RPM. The even mode, characterized by a 0° phase shift between mirrored cavities, reaches a local maximum along the symmetry plane. The odd mode, which corresponds to 180° phase shift between horizontally symmetric cavities, produces a null in the same plane. Thus, the boundary conditions are

$$\frac{dE_y}{dx} = 0 \text{ at } x = -h_2 \text{ (even)}, \tag{1}$$

$$E_y = 0 \text{ at } x = -h_2 \text{ (odd)}. \tag{2}$$

The propagation constant for the (x) direction, denoted as γ_n in expressions (3)–(5), is defined in terms of β_n as $\gamma_n = \sqrt{\beta_n^2 - \left(\frac{\omega}{c}\right)^2}$. The dispersion relation for an infinitely long set of identical cavities is solved by matching the impedance at both boundary I-II and boundary I-III in Fig. 4.[6,13,14] A constant electric field is assigned across these boundaries in order to simplify the matching conditions. The use of a divergent fringing RF electric field, which resulted from the sharp corners at the mouth of the cavities, would modify the cold tube frequency at most by 3% for the first 4 radial modes of a cylindrical magnetron waveguide, as demonstrated in Appendix B of Ref. 15. The detailed derivation for the even mode dispersion relation is found in Appendix A. It should be noted that the TM mode is not considered in this derivation because its dominant electric field is orthogonal to the E × B drifts of the electrons and is therefore unimportant to magnetron operation.

Even mode dispersion relation:

$$\mathrm{UV} = -\mathrm{YZ}, \tag{3a}$$

$$\mathrm{V} = \sin\left(\frac{\omega h_2}{c}\right) + \cos\left(\frac{\omega h_2}{c}\right) \sum_{n=-\infty}^{\infty} \frac{\omega}{\gamma_n c} \frac{w_2}{L} \times \mathrm{sinc}^2\left(\frac{\beta_n w_2}{2}\right) \coth(\gamma_n b), \tag{3b}$$

$$\mathrm{U} = \cos\left(\frac{\omega h}{c}\right) - \sin\left(\frac{\omega h}{c}\right) \sum_{n=-\infty}^{\infty} \frac{\omega}{\gamma_n c} \frac{w_1}{L} \times \mathrm{sinc}^2\left(\frac{\beta_n w_1}{2}\right) \coth(\gamma_n b), \tag{3c}$$

$$\mathrm{Z} = \frac{w_1}{L} \sum_{n=-\infty}^{\infty} \frac{\omega}{\gamma_n c} \frac{\sin\left(\frac{\omega h}{c}\right)}{\sinh(\gamma_n b)} \mathrm{sinc}\left(\frac{\beta_n w_2}{2}\right) \mathrm{sinc}\left(\frac{\beta_n w_1}{2}\right), \tag{3d}$$

$$\mathrm{Y} = \frac{w_2}{L} \sum_{n=-\infty}^{\infty} \frac{\omega}{\gamma_n c} \frac{\cos\left(\frac{\omega h_2}{c}\right)}{\sinh(\gamma_n b)} \mathrm{sinc}\left(\frac{\beta_n w_2}{2}\right) \mathrm{sinc}\left(\frac{\beta_n w_1}{2}\right). \tag{3e}$$

The odd mode dispersion relation is similarly obtained. It reads

Odd mode dispersion relation:

$$\mathrm{UV} = \mathrm{YZ}, \tag{4a}$$

$$\mathrm{V} = \cos\left(\frac{\omega h_2}{c}\right) - \sin\left(\frac{\omega h_2}{c}\right) \sum_{n=-\infty}^{\infty} \frac{\omega}{\gamma_n c} \frac{w_2}{L} \times \mathrm{sinc}^2\left(\frac{\beta_n w_2}{2}\right) \coth(\gamma_n b), \tag{4b}$$

$$\mathrm{U} = \cos\left(\frac{\omega h}{c}\right) - \sin\left(\frac{\omega h}{c}\right) \sum_{n=-\infty}^{\infty} \frac{\omega}{\gamma_n c} \frac{w_1}{L} \times \mathrm{sinc}^2\left(\frac{\beta_n w_1}{2}\right) \coth(\gamma_n b), \tag{4c}$$

$$\mathrm{Z} = \frac{w_1}{L} \sum_{n=-\infty}^{\infty} \frac{\omega}{\gamma_n c} \frac{\sin\left(\frac{\omega h}{c}\right)}{\sinh(\gamma_n b)} \mathrm{sinc}\left(\frac{\beta_n w_2}{2}\right) \mathrm{sinc}\left(\frac{\beta_n w_1}{2}\right), \tag{4d}$$

$$\mathrm{Y} = \frac{w_2}{L} \sum_{n=-\infty}^{\infty} \frac{\omega}{\gamma_n c} \frac{\sin\left(\frac{\omega h_2}{c}\right)}{\sinh(\gamma_n b)} \mathrm{sinc}\left(\frac{\beta_n w_2}{2}\right) \mathrm{sinc}\left(\frac{\beta_n w_1}{2}\right). \tag{4e}$$

In the limit that the slot width w_2 approaches zero, forming a solid cathode, the function Y tends to be 0 in Eq. (4e). Since the relation (V) is finite in this limit, the function (U) must also be zero to satisfy Eq. (4a). Setting the LHS of Eq. (4c) equal to zero allows for the recovery of the classic planar cavity dispersion relation[13,14]

$$\cot\left(\frac{\omega h}{c}\right) = \sum_{n=-\infty}^{\infty} \frac{\omega}{\gamma_n c} \left(\frac{w_1}{L} \mathrm{sinc}^2\left(\frac{\beta_n w_1}{2}\right) \coth(\gamma_n b)\right). \tag{5}$$

The solutions for Eqs. (3) and (4) are validated using the finite element field solver High Frequency Structure Simulator (HFSS).[16] The simulation geometry is setup by creating a cavity set (a single cavity from the top and bottom oscillator) and applying a pair of master-slave boundary conditions (Fig. 5) at $y = \pm L/2$. These boundary conditions are defined by a designated RF phase shift across the structure and are used to isolate only the modes with a given propagation constant (β_0) in (y). A parameter sweep is performed by setting the slave boundary to a variable phase delay and swept from 0 to 360° to represent all possible modes that could exist in an N cavity array as N goes to infinity, where N is the number of cavities. The simulated case was designed to resemble the existing RPM-12a anode at the University of Michigan,[3] with parameters listed in Table I.

The RPM-12a is an un-capped resonant structure specifically designed to mitigate axial variation in the electric field.[6] Therefore, the infinitely uniform axial electric field profile assumed in our 2D analytic model matches well with the actual resonant frequency of the RPM-12a. The resonant frequency and mode separation between even and odd π-modes are relatively constant for variations in axial length of the anode. Higher order axial modes are undesirable for magnetron operation and are not considered in this study.

The resultant frequencies obtained from the numerical eigenmode search and from the analytic dispersion solutions

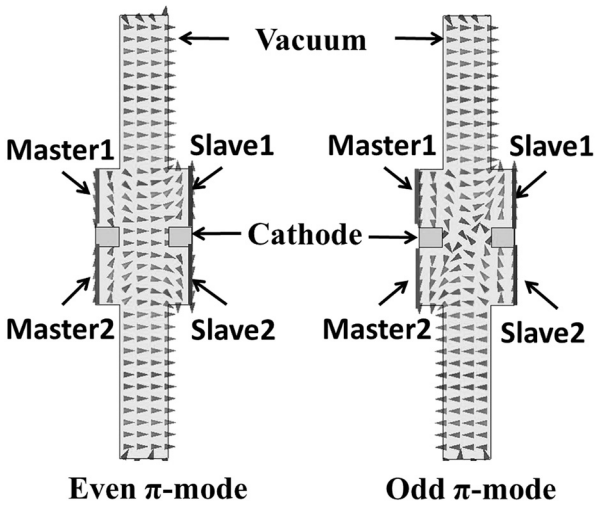

FIG. 5. Front facing perspective of two separate cavities in HFSS illustrating the boundary conditions as well as the electric field vectors for the even (left) and odd (right) π-modes.

(Eqs. (3a) and (4a)) as a function of phase shift per cavity are plotted in Fig. 6, where $\beta_0 = 2\pi/\lambda_g = 2\pi(\delta\phi)/(360 * L)$, $(\delta\phi)$ is the phase shift per cavity in degrees, and λ_g is the guide wavelength. General agreement is noticed.

This analysis is applied to mode separation by selecting a primary mode (π-mode) and numerically solving for the difference in frequency between the even and odd dispersion solutions. We calculate the difference in the two resonant frequencies as a function of cathode height (h_2) in Fig. 7(a), cathode slot width (w_2) in Fig. 7(b), and AK gap (b) in Fig. 7(c).

Figs. 7(a)–7(c) show that the separation between even and odd π-modes decreases monotonically with increasing cathode thickness (h_2) or AK gap (b) while there exists an optimal cathode slot width (w_2) between $w_2 = 0$ (no slot) and $w_2 = \lambda_\pi/2 = L$ (no cathode). Under realistic parameters (AK gap $>$ 1 cm) even-odd mode separation can theoretically reach 100 MHz, but this separation is reduced as the AK gap is increased past 1 cm. Long-pulse relativistic devices typically require larger AK-gaps due to plasma expansion from the cathode and subsequent gap closure in the diode, which may limit pulse duration or mode separation.

IV. ELECTROMAGNETIC PARTICLE IN CELL MODELING OF THE MODE CONTROL CATHODE

The MCC, in addition to providing enhanced mode discrimination, will act to prime the π-mode operation via the periodic emission structures.[12] It also offers additional mode

TABLE I. University of Michigan, RPM-12a, experimental geometry and dimensions.

Cavity width (w_1)	0.0192 m
AK gap (b)	0.024 m
Cathode slot width (w_2)	0.02 m
Cavity height (h)	0.063 m
Cathode half height (h_2)	0.004 m
Axial depth (z)	0.11 m
Periodicity (L)	0.0384 m

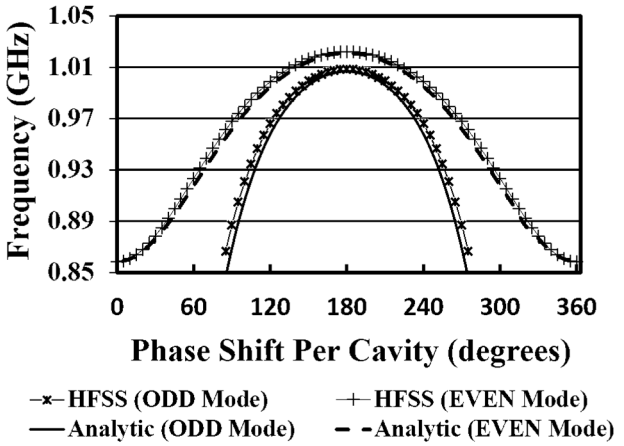

FIG. 6. Analytic (solid line) and simulated (x-marker) dispersion relations for the even and odd π-modes.

stability through cross-oscillator coupling. Analysis of this concept is performed by simulating the RPM-12a anode structure in the 2D particle in cell code, MAGIC. Re-entrant boundary conditions are imposed on either end of a 6-cavity model,[17] in order to artificially remove secondary cross oscillator coupling mechanisms, such as coupling through the cylindrical recirculation regions, and establish the MCC as the primary source of communication between each planar cavity array. The recirculation sections, independently from

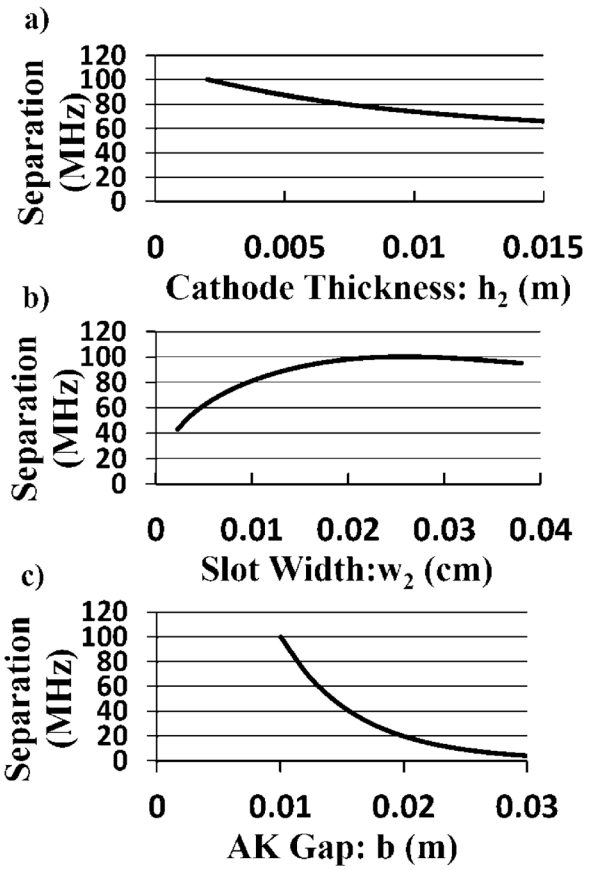

FIG. 7. Analytic mode separation results between the even and odd pi-modes; (a) varying parameter: h_2, set $w_2 = 0.024$ m, AK = 0.01 m; (b) varying parameter: w_2, set $h_2 = 0.002$ m, AK = 0.01 m; (c) varying parameter: b, set $w_2 = 0.024$ m, $h_2 = 0.002$ m.

the MCC, provide a boundary condition that supports mode separation between "even" and "odd" operating modes. Mode separation, in these cases (using a solid cathode), is typically much less than with the MCC suggesting its impact is limited. Additionally, this section is not as dynamic or tunable as the MCC as it must also be designed to minimally affect space charge spoke propagation and limit desynchronization of the beam and RF wave.

Each simulation used an applied voltage of −300 kV for 300 ns on either a solid conducting cathode (Fig. 8(a)), to isolate the two sides, or the MCC (Figs. 8(b) and 8(c)) with a slotted geometry. The MCC's geometry is described by the following parameters: AK gap (b) of 2.4 cm, cathode slot width (w_2) of 1.92 cm, and cathode height (h_2) of 0.5 cm. Each simulated case applied a different axial magnetic field, which varied from 0.1 T to 0.35 T in order to observe several excitable modes in the RPM.

The principal operating modes identified in this study were the 4π/6, π-even (Fig. 8(b)), π-odd (Fig. 8(c)), 7π/6, and 8π/6 modes. Note that the even-π mode, despite the symmetry in the RF electric field, displays anti-symmetric spoke formation due to the $E_{RF} \times B$ drift vector. The simulated results, for the MCC, are plotted against the theoretical Buneman-Hartree condition in Fig. 9, which reads[9,18–20] (β is the phase velocity of the mode in units of the speed of light)

$$\frac{eV}{mc^2} = \frac{eBb}{mc}\beta - [1 - (1 - \beta^2)^{\frac{1}{2}}]. \quad (6)$$

The π-mode field configuration was the dominant mode structure for magnetic fields between 0.12 T and 0.27 T, far surpassing the range predicted by the planar Bunemann-Hartree theory. Neighboring modes including 7π/6 and 8π/6 developed at applied fields of 0.28 T and 0.33 T, respectively. The solid conducting cathode results (not shown) demonstrated π-mode operation between 0.15 T and 0.20 T, outside of which severe competition with neighboring modes was evident. The enhanced mode stability provided by the MCC is largely dependent on the presence of cross oscillator coupling as local perturbations imposed on one side of the device can be readily corrected by stable operation of the other side and vice versa. The extent of this coupling can be directly controlled by manipulating the geometry of the cathode to vary the amount of RF power coupled between the top and bottom slow wave structures.

A series of simulations were performed in which the AK gap (b) was linearly varied from 1.0 cm to 3.2 cm in order to alter the magnitude of the transverse electric field (E_y) at the cathode. Since the device exhibits some duality between operating as two separate oscillators and a single resonant structure, initial mode development may sometimes lack phase coherency between the two sides. Due to this phenomenon, both oscillation start-up times and phase locking times were monitored for each simulated case. In this study, oscillators are considered locked when the relative phase between

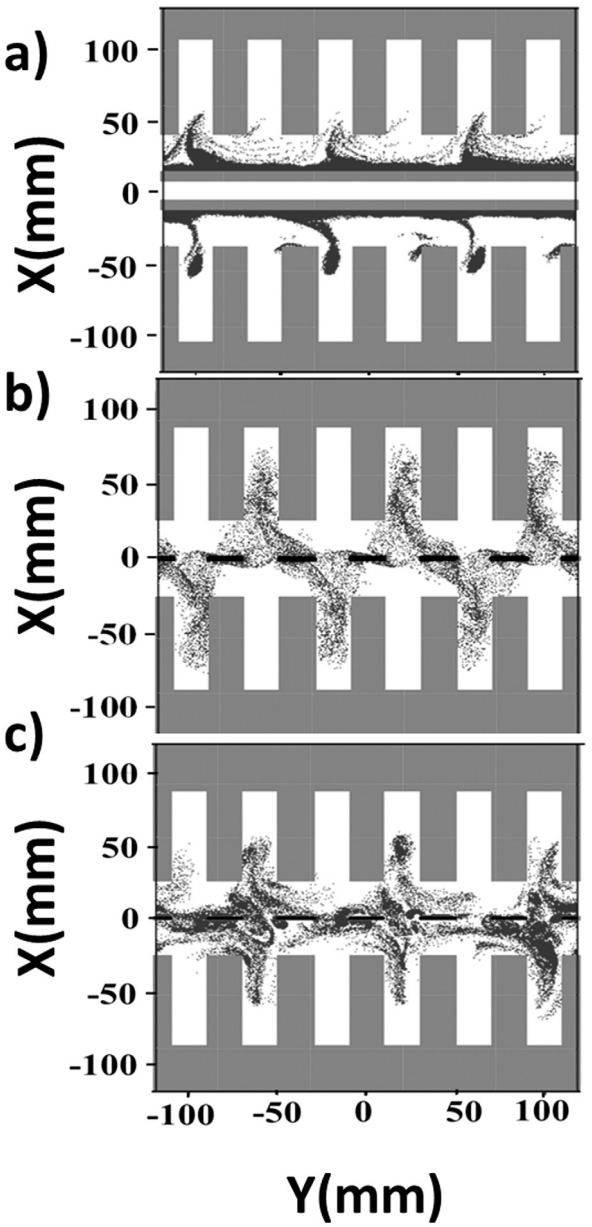

FIG. 8. MAGIC PIC phase space images: (a) solid cathode π-mode spoke formation, (b) even π-mode spoke formation using the MCC, and (c) odd π-mode spoke formation using the MCC.

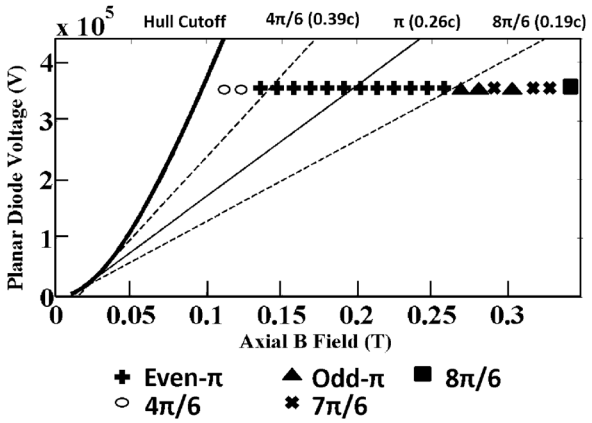

FIG. 9. Simulated results from MAGIC PIC plotted against the relativistic planar Bunemann-Hartree conditions for different modes, with the phase velocity labeled in parenthesis (5π/6 and 7π/6 curves, which exist between 4π/6 and 8 π/6, are not shown).

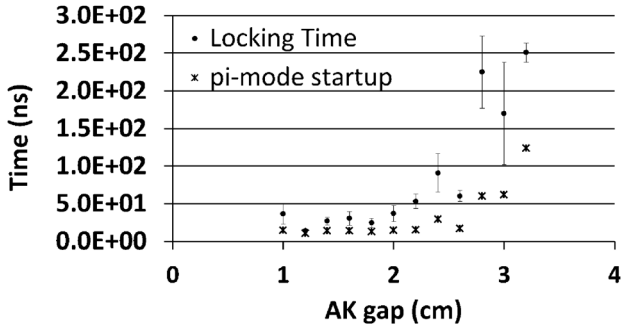

FIG. 10. Simulated results showing oscillation start up times (x) and phase locking times (dots) as a function of the AK gap.

two mirrored cavities on the top and bottom does not vary more than $\pm 2^\circ$ for 50 ns.[21–23] Simulations were modeled using a 0.18 T uniform axial magnetic field (B) for 300 ns and the applied voltage (V) was varied to scale the electric field as dictated by Bunemann-Hartree condition for the even π-mode in a planar diode (-150 kV to -500 kV). All simulations, which achieved locking using the MCC, operated in the even π-mode electric field configuration shown in Fig. 8(b), the odd π-mode fields (Fig. 8(c)) are resonant at lower phase velocities and were easily isolated from this portion of the study.

The simulated control case (Fig. 8(a)), with a solid aluminum cathode and 2.4 cm AK gap, demonstrated π-mode oscillations after approximately 100 ns but never fully satisfied the locking condition over the course of the 300 ns simulation. The MCC was not only able to readily produce π-mode oscillations in less than 30 ns, under the same operating conditions, but also reached a phase-locked state between opposing slow wave structures in less than 100 ns. The trend of relative start up times (defined as the time required for the magnetron to produce π-mode space charge spoke formations whose height exceeded the AK gap) and locking times as a function of AK gap are shown in Fig. 10.

The time required for the top and bottom oscillators to lock increases exponentially with the AK gap varying from, approximately 30 ns at $b = 0.012$ m to 250 ns at $b = 0.032$ m. In the limit that the AK gap goes to zero, the 12-cavity slow wave structure more closely resembles 6 isolated resonators that by definition share the same frequency and phase. Resonant structures with small AK gaps ($b \ll w_1$), however, demonstrate a strong disparity between the RF fields under vanes versus under the cavities and often fail to develop a stable operating mode.

V. CONCLUDING REMARKS

Theory and simulation show that the mode control cathode is a practical means of enhancing mode separation, improving start up times, and enabling cross-oscillator coherency in the recirculating planar magnetron. The application of this concept is largely dependent on both the geometry of the cathode and anode and may have diminishing utility in diodes with large separation between anode and cathode.

RF extraction was not studied here as we focus on the effect of the cathode on the RF dispersion and mode development. The inclusion of an extractor scheme is anticipated to heavily reduce the Q of the RPM and improve overall locking time of the device as locking time is typically proportional to Q.[21–23]

Experiments are underway to employ the MCC in the experimental RPM-12a at the University of Michigan. Calibrated B-dot loops, measuring mirrored cavities on the top and bottom oscillators, are used to diagnose phase locking.

ACKNOWLEDGMENTS

This work was supported by the Air Force Office of Scientific Research under Grant No. FA9550-10-1-0104, the Air Force Research Laboratory, and L-3 Communications Electron Devices.

APPENDIX: EVEN MODE DISPERSION

This appendix establishes the dispersion relation (3a) for the even π-mode for the mode control cathode in an infinite array of cavities in a planar magnetron. The odd mode solution is established similarly. Referring to the geometry displayed in Fig. 4, the electromagnetic solution is divided into three distinct regions: AK gap-I, cathode slot-II, and cavity-III.

Region 1: $0 < x < b$ and $-L/2 < y < L/2$

$$H_z = je^{j\omega t} \sum_{n=-\infty}^{\infty} [A_n \cosh(\gamma_n x) + A'_n \sinh(\gamma_n x)]\ e^{-j\beta_n y}, \quad \text{(A1)}$$

$$j\omega\epsilon E_x = -\beta_n j e^{j\omega t} \sum_{n=-\infty}^{\infty} [A'_n \cosh(\gamma_n x) + A_n \sinh(\gamma_n x)] \times e^{-j\beta_n y}, \quad \text{(A2)}$$

$$j\omega\epsilon E_y = -e^{j\omega t} \sum_{n=-\infty}^{\infty} [A'_n \gamma_n \cosh(\gamma_n x) + A'_n \gamma_n \sinh(\gamma_n x)] \times e^{-j\beta_n y}. \quad \text{(A3)}$$

Region 2: $-h_2 < x < 0$ and $-w_2/2 < y < w_2/2$

$$E_y = \left[B' \sin\left(\frac{\omega(x+h_2)}{c}\right) + B\cos\left(\frac{\omega(x+h_2)}{c}\right)\right], \quad \text{(A4)}$$

$$-j\omega\mu H_z = \frac{\omega}{c}\left[B' \cos\left(\frac{\omega(x+h_2)}{c}\right) - B\sin\left(\frac{\omega(x+h_2)}{c}\right)\right]. \quad \text{(A5)}$$

Region 3: $b < x < d$ and $-w_1/2 < y < w_1/2$

$$E_y = e^{j\omega t} D \sin\left(\frac{\omega(x-d)}{c}\right), \quad \text{(A6)}$$

$$-j\omega\mu H_z = \frac{D\omega}{c}\cos\left(\frac{\omega(x-d)}{c}\right). \quad \text{(A7)}$$

The degeneracy experienced by the RPM can be isolated (to either the even or the odd mode) analytically by the boundary condition applied at the horizontal plane of symmetry

($x = -h_2$). The even mode, whose electric field E_{yII} experiences a local maxima where the derivative $dE_y/dx = 0$. Applying this boundary condition to the TEM solution presented in Eqs. (A4) and (A5) we can obtain the following:

$$E_{yII} = B\cos\left(\frac{\omega(x+h_2)}{c}\right), \tag{A8}$$

$$-j\omega\mu H_{zII} = -B\frac{\omega}{c}\sin\left(\frac{\omega(x+h_2)}{c}\right). \tag{A9}$$

Treating the cavity as a shorted parallel plate transmission line, the RF field at the vane tips reads

$$E_{yIII} = D\sin\left(\frac{\omega(b-d)}{c}\right). \tag{A10}$$

Resonance is achieved by matching the impedance at each interface (I-II and I-III). Classically this impedance matching is performed by ensuring continuity of the point-wise electric field E_y and average magnetic field B_z across the boundary. The RF electric fields in the AK gap (region I) is represented as a summation of an infinite combination of spatial harmonics in (A3) must therefore be set equal to the value of the of the cavity field (E_{yIII}) at the I-III interface ($x = b$)

$$-D\sin\left(\frac{\omega h}{c}\right) = \sum_{n=-\infty}^{\infty}\frac{-\gamma_n}{j\omega\varepsilon}e^{-j\beta_n y}[A_n\sinh(\gamma_n b) + A'_n\cosh(\gamma_n b)]. \tag{A11}$$

Applying Fourier analysis over the period L the following expression relating the coefficients (A_n, A'_n, D) is obtained. Let

$$\frac{-\gamma_n}{j\omega\varepsilon}[A_n\sinh(\gamma_n b) + A'_n\cosh(\gamma_n b)] = D\frac{w_1}{L}\sin\left(\frac{\omega h}{c}\right)\mathrm{sinc}(\theta_1), \tag{A12}$$

where $\mathrm{sinc}(x) = \frac{\sin(x)}{x}$. We define $\theta_1 = \beta_n\ w_1/2$ and $\theta_2 = \beta_n\ w_2/2$.

In a similar fashion E_y must also be continuous across the I-II boundary at $x = 0$, relating (A'_n, B) upon setting $B' = 0$ in Eq. (4a) for the even mode.

$$\frac{-\gamma_n}{j\omega\varepsilon}A'_n = B\frac{w_2}{L}\cos\left(\frac{\omega h_2}{c}\right)\mathrm{sinc}(\theta_2). \tag{A13}$$

The average magnetic field, H_{ZI} and H_{zIII}, must be equal across the I-III interface which is performed by integrating (A1) with respect to (y) from $y = -w_1/2$ to $y = w_1/2$ and dividing by w_1. Equation (A14) relates the coefficients (A_n, A'_n, D)

$$\frac{-1}{j\mu}\frac{D}{c}\cos\left(\frac{\omega h}{c}\right) = \sum_{n=-\infty}^{\infty}[A_n\cosh(\gamma_n b) + A'_n\sinh(\gamma_n b)]\,\mathrm{sinc}(\theta_1). \tag{A14}$$

Applying the same analysis to the magnetic field across the I-II boundary at $x = 0$, relating (A_n, B)

$$\frac{1}{j\mu}\frac{B}{c}\sin\left(\frac{\omega h_2}{c}\right) = \sum_{n=-\infty}^{\infty}A_n\,\mathrm{sinc}(\theta_2). \tag{A15}$$

Using Eq. (A13) solve for the unknown coefficient A'_n

$$A'_n = \frac{-j\omega\varepsilon B}{\gamma_n}\frac{w_2}{L}\cos\left(\frac{\omega h_2}{c}\right)\mathrm{sinc}(\theta_2). \tag{A16}$$

The expression determined in Eq. (A16) may then be plugged directly into Eq. (A12) to yield

$$A_n = \frac{Dj\omega\epsilon}{\gamma}\left[\frac{w_1}{L}\sin\left(\frac{\omega h}{c}\right)\frac{\mathrm{sinc}(\theta_1)}{\sinh(\gamma_n b)}\right] + \frac{j\omega\varepsilon B}{\gamma_n}\frac{w_2}{L}\cos\left(\frac{\omega h_2}{c}\right)\mathrm{sinc}(\theta_2)\coth(\gamma_n b). \tag{A17}$$

Using Eqs. (A16) and (A17), the bracket in the RHS of Eq. (A14) can be expressed in terms of the coefficients of the cavity field (D) and the cathode field (B):

$$\begin{aligned}A_n\cosh(\gamma_n b) + A'_n\sinh(\gamma_n b) = {} & \frac{Dj\omega\epsilon}{\gamma_n}\left[\frac{w_1}{L}\sin\left(\frac{\omega h}{c}\right)\right.\\ & \left.\times\mathrm{sinc}(\theta_1)\coth(\gamma_n b)\right] + \frac{j\omega\varepsilon B}{\gamma_n}\left[\frac{w_2}{L}\cos\left(\frac{\omega h_2}{c}\right)\right.\\ & \times\mathrm{sinc}(\theta_2)\coth(\gamma_n b)\cosh(\gamma_n b) - \frac{w_2}{L}\cos\left(\frac{\omega h_2}{c}\right)\\ & \left.\times\mathrm{sinc}(\theta_2)\sinh(\gamma_n b)\right].\end{aligned} \tag{A18}$$

Upon using the hyperbolic trigonometric identity $\cosh^2(x) - \sinh^2(x) = 1$ for all x, Eq. (A18) becomes,

$$\begin{aligned}A_n\cosh(\gamma_n b) + A'_n\sinh(\gamma_n b) = {} & \frac{Dj\omega\epsilon}{\gamma_n}\left[\frac{w_1}{L}\sin\left(\frac{\omega h}{c}\right)\right.\\ & \left.\times\mathrm{sinc}(\theta_1)\coth(\gamma_n b)\right] + \frac{j\omega\varepsilon B}{\gamma_n}\left[\frac{w_2}{L}\cos\left(\frac{\omega h_2}{c}\right)\frac{\mathrm{sinc}(\theta_2)}{\sinh(\gamma_n b)}\right].\end{aligned} \tag{A19}$$

Putting Eq. (A19) into Eq. (A14), we have

$$\begin{aligned}-\frac{D\cos\left(\frac{\omega h}{c}\right)}{j\mu c} = \sum_{n=-\infty}^{\infty}\frac{j\omega\epsilon}{\gamma_n}\left[D\left(\frac{w_1}{L}\sin\left(\frac{\omega h}{c}\right)\right.\right.\\ \left.\times\mathrm{sinc}(\theta_1)\coth(\gamma_n b)\right)\\ \left.+ B\left(\frac{w_2}{L}\cos\left(\frac{\omega h_2}{c}\right)\frac{\mathrm{sinc}(\theta_2)}{\sinh(\gamma_n b)}\right)\mathrm{sinc}(\theta_1)\right].\end{aligned} \tag{A20}$$

Pulling all the terms with the coefficient D to one side and replacing the following relation for the speed of light $c = \frac{1}{\sqrt{(\mu_0\epsilon_0)}}$, Eq. (A20) is written as

$$D * U = B * Y. \tag{A21}$$

Providing the same analysis with Eq. (A11) and using Eqs. (A16) and (A17), we obtain

$$B * V = -D * Z, \tag{A22}$$

where U, V, Y, and Z are

$$V = \sin\left(\frac{\omega h_2}{c}\right) + \cos\left(\frac{\omega h_2}{c}\right) \sum_{n=-\infty}^{\infty} \frac{\omega}{\gamma_n c} \frac{w_2}{L} \mathrm{sinc}^2(\theta_2) \coth(\gamma_n b), \tag{A23a}$$

$$U = \cos\left(\frac{\omega h}{c}\right) - \sin\left(\frac{\omega h}{c}\right) \sum_{n=-\infty}^{\infty} \frac{\omega}{\gamma_n c} \left(\frac{w_1}{L} \mathrm{sinc}^2(\theta_1) \coth(\gamma_n b)\right), \tag{A23b}$$

$$Z = \frac{w_1}{L} \sum_{n=-\infty}^{\infty} \frac{\omega}{\gamma_n c} \frac{\sin\left(\frac{\omega h}{c}\right)}{\sinh(\gamma_n b)} \mathrm{sinc}(\theta_2) \mathrm{sinc}(\theta_1), \tag{A23c}$$

$$Y = \frac{w_2}{L} \sum_{n=-\infty}^{\infty} \frac{\omega}{\gamma_n c} \frac{\cos\left(\frac{\omega h_2}{c}\right)}{\sinh(\gamma_n b)} \mathrm{sinc}(\theta_2) \mathrm{sinc}(\theta_1). \tag{A23d}$$

Multiply (A21) and (A22), cancel the like (D*B) term on both sides of the equation to yield the dispersion relation (3a)

$$UV = -YZ. \tag{A24}$$

[1]R. M. Gilgenbach, Y. Y. Lau, D. M. French, B. W. Hoff, M. Franzi, and J. Luginsland, "Recirculating planar magnetrons for high-power high-frequency radiation generation," IEEE Trans. Plasma Sci. **39**(4), 980–987 (2011).

[2]R. M. Gilgenbach, Y. Y. Lau, D. M. French, B. W. Hoff, and M. Franzi, "Crossed field device," U.S. 2011/0204785 A1, Aug. 25, 2011 patent pending.

[3]M. A. Franzi, R. M. Gilgenbach, B. W. Hoff, D. Chalenski, D. H. Simon, Y. Y. Lau, and J. Luginsland "Recirculating planar magnetron simulation and experiment," IEEE Trans. Plasma Sci. (in press, 2013).

[4]B. W. Hoff, M. A. Franzi, D. M. French, G. Greening, and R. M. Gilgenbach, "A compact, Pi-mode extraction scheme for the axial B-field recirculating planar magnetron," AFRL-RD-PS (TR-2012-0039) 23 Jun 2012.

[5]T. A. Spencer, "Current HPM source research," in *Proceedings of the 6th Workshop on High Energy Density and High Power RF* (AIP, Berkeley Springs, West Virginia, 2003), p. 46.

[6]G. B. Collins, *Microwave Magnetrons* (McGraw-Hill, New York, 1948).

[7]R. M. Gilgenbach, Y. Y. Lau, H. McDowell, K. L. Cartwright, and T. A. Spencer, "Crossed-field devices," in *Modern Microwave and Millimeter Wave Power Electronics*, edited by R. J. Barker, N. C. Luhmann, J. H. Booske, and G. S. Nusinovich (IEEE, Piscataway, NJ, 2004), Chap. 6.

[8]A. S. Gilmour, *Microwave Tubes* (Artech House, 1986), pp. 348–379.

[9]J. Benford, J. A. Swegle, and E. Schamiloglu, *High Power Microwaves* (CRC, 2007).

[10]R. W. Lemke, T. C. Genoni, and T. A. Spencer, "Effects that limit efficiency in relativistic magnetrons," IEEE Trans. Plasma Sci. **28**(3), 887–897 (2000).

[11]M. Fuks and E. Schamiloglu, "Rapid start of oscillations in a magnetron with a 'transparent' cathode," Phys. Rev. Lett. **95**(20), 205101 (2005).

[12]M. C. Jones, V. B. Neculaes, Y. Y. Lau, R. M. Gilgenbach, and W. M. White, "Cathode priming of a relativistic magnetron," Appl. Phys. Lett. **85**, 6332 (2004).

[13]Y. Y. Lau and D. Chernin, "A review of AC space charge effect in electron circuit interactions," Phys. Fluids B **4**(11), 3473–3497 (1992).

[14]J. W. Gewartowski and H. A. Watson, *Principles of Electron Tubes: Including Grid-Controlled Tubes, Microwave Tubes, and Gas Tubes* (Van Nostrand, 1965).

[15]Y. Y. Lau and L. R. Barnett, "Theory of a low magnetic field gyrotron (gyromagnetron)," Int. J. Infrared Millim. Waves **3**(5), 619–644 (1982).

[16]See http://www.ansoft.com/products/hf/hfss/ for information regarding software capabilities and solution algorithms.

[17]L. D. Ludeking, G. E. Thomas, and W. M. Bollen, "Simulation and analysis of a reentrant planar magnetron," in International Electron Devices Meeting, Washington, D.C., Dec. 6–9, 1987, Vol. 33, pp. 160–163.

[18]R. C. Davidson, G. L. Johnston, K. T. Tsang, and A. T. Drobot, "Cylindrical Brillouin flow in relativistic smooth-bore magnetrons," *presented at the Society of Photo-Optical Instrumentation Engineers (SPIE) Conference Series*, Bellingham, WA, 1989, Vol. 1061, pp. 186–200.

[19]Y. Y. Lau, J. W. Luginsland, K. L. Cartwright, D. H. Simon, W. Tang, B. W. Hoff, and R. M. Gilgenbach, "A re-examination of the Buneman-Hartree condition in a cylindrical smooth-bore relativistic magnetron," Phys. Plasmas **17**, 033102 (2010).

[20]D. H. Simon, Y. Y. Lau, J. W. Luginsland, and R. M. Gilgenbach, "An unnoticed property of the cylindrical relativistic Brillouin flow," Phys. Plasmas **19**(4), 043103–043103–5 (2012).

[21]P. Pengvanich, Y. Y. Lau, E. Cruz, R. M. Gilgenbach, B. Hoff, and J. W. Luginsland, "Analysis of peer-to-peer locking of magnetrons," Phys. Plasmas **15**(10), 103104–103104–4 (2008).

[22]W. Woo, J. Benford, D. Fittinghoff, B. Harteneck, D. Price, R. Smith, and H. Sze, "Phase locking of high power microwave oscillators," J. Appl. Phys. **65**(2), 861–866 (1989).

[23]R. Adler, "A study of locking phenomena in oscillators," Proc. IRE **34**(6), 351–357 (1946).